Journal of Applied Polymer Science

Morphology evolution of a thermotropic liquid-crystalline polymer in a polyamide 6,6 matrix regulated by graphene

Mingming Wang, Yuanshi Xin, Chao Su, Feng Xue, Fanglin Xu, Tongsheng Li

State Key Laboratory of Molecular Engineering of Polymers, Collaborative Innovation Center of Polymers and Polymer Composite Materials, Department of Macromolecular Science, Fudan University, Shanghai 200433, China

Correspondence to: T. Li (E-mail: lits@fudan.edu.cn)

ABSTRACT: A two-step process, thermotropic liquid-crystalline polymer (TLCP) premixing with reduced graphene oxide (RGO) followed by blending with polyamide 6,6 (PA66), was used to prepare ternary TLCP/RGO/PA66 blends. The rheological behaviors, morphology, and mechanical properties of the blends were investigated. The results show that RGO migrated from the TLCP phase to the interface between the TLCP and PA66 phase during melt blending; this was due to a similar affinity of the RGO nanosheets to both component polymers. The dimensions of the dispersive TLCP domains were markedly reduced with the mounting RGO content; this revealed a good compatibilization effect of RGO on the immiscible polymers. The hierarchical structures of the TLCP fibrils were found in both the unfilled TLCP/PA66 blends and TLCP/RGO/PA66 blends. This supposedly resulted from the extensional and torsional action of unstable capillary flow. With the addition of RGO, the viscosities of the blends decreased further, and the fibrillation of TLCP and the mechanical performance of TLCP composites were both enhanced. © 2016 Wiley Periodicals, Inc. J. Appl. Polym. Sci. **2016**, *133*, 43735.

KEYWORDS: graphene and fullerenes; liquid crystals; morphology; nanotubes; rheology; structure–property relations

Received 26 January 2016; accepted 4 April 2016

DOI: 10.1002/app.43735

INTRODUCTION

Since Kiss[1] introduced the conception of *in situ* composites containing thermotropic liquid-crystalline polymers (TLCPs) and thermoplastics (TPs) in the 1980s, the field has attracted much attention in scientific research and for industrial applications. TLCPs are essentially rigid-rod main-chain nematic polymers incorporated with some irregularity or flexibility to decrease the melting point below the decomposition temperature.[2] The rigid rodlike molecular structure allows these materials to exhibit molecular order in a liquid mesophase and endows them with excellent processability, unique mechanical properties, and high thermal and chemical stability. The blending of TLCPs with conventional polymers is a novel approach for reinforcing polymer matrixes compared to fiber-reinforced polymers. The addition of small amounts of TLCPs could result in a dramatic decrease in the viscosity of matrixes. Furthermore, the dispersive TLCP phase can deform into long fibrils along the direction of the melt flow to reinforce the matrixes under appropriate processing conditions.

Many TLCP blends have been investigated in the last 2 decades; these include polyolefin, polyamides, polyesters, polyimides, polycarbonates, polysulfone, poly(phenylene sulfide), and ultra-high-molecular-weight polyethylene.[3–15] These studies have mainly focused on the morphology, rheology, compatibility, mechanical properties, crystallization behavior, and orientation parameter of the blends. Despite the advantages of the TLCP blends, the actual mechanical performances proved far more than satisfactory, particularly at a low TLCP contents.[3,9,13] This was mainly because of the poor interfacial adhesion resulted from the incompatibility between TLCP and the matrix and the imperfect fibrillation of the TLCP phase.

Generally, the interfacial adhesion can be enhanced through the addition of compatibilizers or reactive extrusion.[16–20] Tjong and coworkers[17,18] prepared TLCP/polyamide 6 (PA6) composites compatibilized by maleated polypropylene and a random styrene–maleic anhydride copolymer with injection molding. Significant improvements in the static tensile properties and impact properties were obtained. Caligiuri *et al.*[20] investigated the thermal behaviors, mechanical and physical properties, and morphology of the reactive blending of poly(ethylene 2,6-naphthalate) and TLCP (Vectra A950). They reported that an increased mixing rate or blending time was significant to the improvement of the occurrence of interchange reactions between the blend components; this ensured good adhesion between the matrix and dispersed phase. Moreover, the TLCP domains became smaller with a narrower distribution.

When the TLCP phase deformed into fibrils during the melt processing of ternary blends containing a solid reinforcement,

the blends were named as *in situ* hybrid composites.[21] Great efforts have been made to improve the fibrillation of the TLCP phase in matrix through the addition of conventional inorganic fillers. It is commonly known that the viscosity ratio (λ) of TLCP to the matrix is a critical factor in determining the fibrillation of TLCP. In binary TLCP/TP systems, fibrillation can be enhanced when λ is much lower than unity. Lee *et al.*[2] added silica fillers (SiO_2) to a TLCP/polypropylene system; this served as a viscosity-thickening agent to increase the polypropylene matrix viscosity (η_m) and improve the fibrillation of the TLCP phase. The formation of TLCP fibrils was enhanced with the incorporation of 5–15 wt % silica, and the presence of the TLCP fibrils improved the flow properties of the TLCP/polypropylene/SiO_2 blends. Zhang *et al.*[21] found that nanoclay fillers were well dispersed by a melt-extrusion process when they were added to TLCP/PA6 blends. The TLCP domains got smaller at clay contents of less than 3 wt % and deformed into fibrils at clay contents of up to 5 and 7 wt %. This was attributed to the role of nanoclay as a compatibilizer to improve the interfacial adhesion and to suppress the interfacial slip between TLCP and the PA6 phase in the melt, so the shear stress was effectively transferred to the dispersed TLCP phase. Zheng *et al.*[12] prepared ternary PA6/glass fiber/TLCP blends with three kinds of PA6 with different viscosities as matrixes. Their study showed that although no fibrils were generated in binary PA6/TLCP blends, TLCP fibrillated to a large aspect ratio in some ternary blends after the incorporation of glass fibers. They put forward that the fibrillation was promoted by elongational flow at the entrance of the capillaries instantaneously formed by stacked glass fibers.

Numerous TLCP/TP blends with all kinds of added inorganic fillers serving as third components have been reported; these fillers include SiO_2, clay, glass fibers, glass beads, carbon nanofibers, and carbon fibers.[12–15,21–25] However, we did not find any study examining a TLCP/TP system with graphene. It is well known that graphene is composed of a planar monolayer of conjugated sp^2 carbon atoms bonded into six-membered rings.[26] It is the thinnest material that has been discovered in the world and has a single-layer thickness of less than 1 nm. Single-layered graphene is also the strongest material; it exhibits a Young's modulus of 1100 GPa and a tensile strength of 130 GPa.[27] Graphene can be directly incorporated with polymers as a reinforcing filler in the preparation of nanocomposites. Kalaitzidou *et al.*[28] prepared exfoliated graphite nanoplatelet/polyurethane composites by melt blending. When oriented properly, the exfoliated graphite nanoplatelets not only stiffened the composites but also reduced the coefficient of thermal expansion in two directions rather than in one as in the case of aligned fiber composites. Compared with other commercial reinforcing fillers, such as carbon fibers, carbon black, and clays, the smaller aspect ratio of graphene nanosheets showed better compatibility with the polymer and favored the formation of more uniform composites.

To determine the influence of graphene on TLCP blends, we prepared ternary TLCP/graphene/polyamide 6,6 (PA66) blends and set TLCP as the minor phase. PA66 was chosen as the matrix because of its similar processing temperature compared with TLCP (Vectra A950). In addition, the formation of TLCP fibrils in the low-viscous PA66 matrix involved much difficulty, so the determination of the role of graphene on fibrillation was elaborate. There was a distinctive processing order that reduced graphene oxide (RGO) premixed with TLCP instead of the PA66 matrix in this study, which had never been reported in previous literatures. As is well known, the anisotropy of neat TLCPs can be reduced markedly with the incorporation of inorganic fillers.[6,29] Therefore, most researchers have premixed TPs with fillers and then blended TLCPs because of the negative influence on the fibrillation of the TLCP phase. However, we assumed that there was little impact on the anisotropy or orientation parameter of TLCP at a relatively low graphene content because of the unique planar structure of nanoscaled graphene.

EXPERIMENTAL

Materials

The TLCP used was Vectra A950, a commercial thermotropic liquid-crystalline copolyester manufactured by Hoechst Celanese. It was composed of 73 mol % hydroxybenzoic acid and 27 mol % hydroxynaphthoic acid. The PA66 that we used was a product of high molecular weight and medium viscosity and was supplied by Asahi Chemical Industry Co., Ltd. (Japan). The graphene that we used was RGO, which we prepared.

For the synthesis of RGO, a modified Hummers method was used to synthesize graphene oxide (GO) first. The detailed synthetic process can be found elsewhere.[30,31] During the reduction of GO, ammonia solution was added to inhibit the aggregation of the resulting RGO with hydrazine hydrate as the reductant. Finally, RGO powder was obtained from the RGO solution by lyophilization and then heated up to 280 °C in an oven to remove the thermolabile groups.

Processing

Before processing, the polymers and fillers were dried for 24 h *in vacuo* at 110 °C. RGO was first premixed with TLCP at weight ratios of 0.5, 1, 2, and 3% with a Haake Polylab extruder equipped with a pair of homodromy screws. A temperature profile of 255–280–280–280 °C from the hopper to die, respectively, was set. The screw speed was fixed at 30 rpm. The extrudates of the TLCP/RGO mixtures with various RGO contents were pelletized and dried well; this was followed by re-extrusion with PA66 under the same conditions. A fixed TLCP concentration of 10 wt % was used for all of the TLCP/PA66 containing blends. For the processing of the unfilled TLCP/PA66 blends, the first-stage extrusion imposed on neat TLCP was the same as the TLCP/RGO mixtures. The last extrudates were pelletized and dried for rheological tests.

Rheological Measurements

Rheological measurements were conducted with a Haake Polylab single-screw extruder with the function of rheological capillary extrusion. The diameter of the capillary was 1.5 mm, and the length/diameter ratio was 40. The screw speed ranged from 5 to 60 rpm. The shear viscosities of the neat polymers were measured at 285 and 305 °C. The shear viscosities of the polymer blends were measured only at 305 °C. The extrudates were immediately collected in a beaker, and the vertical distance

between the capillary and beaker was no more than 10 cm to ensure that no postdrawing was applied after the extrusion. Both Bagley and Rabinowitsch corrections were applied for all of the data.

IR Spectroscopy Analysis

IR analysis was carried out on a Nexus 470 Fourier transform infrared spectroscopy instrument made by Thermo-Fisher at a resolution of 0.09 cm^{-1}. Wave numbers between 400 and 4000 cm^{-1} were examined. RGO powder and GO powder were investigated by the KBr method.

Wide-Angle X-ray Diffraction

A wide-angle X-ray diffraction test was conducted with a PaNalytical diffractometer with Cu Kα radiation ($\lambda = 0.15406$ nm). The RGO and graphite in powder form were tested.

Thermogravimetric Analysis (TGA)

TGA measurements for the RGO and graphite were performed on a thermogravimetric analyzer (TGA1, Mettler-Toledo, Switzerland) at a heating rate of 20 °C/min under a nitrogen atmosphere from 50 to 800 °C.

Morphological Observation

The extrudates after the rheological tests were cryofractured in liquid nitrogen and sputter-coated with gold. Then, the fracture surfaces were observed with a field-emission scanning electron microscope (Zeiss Ultra 55, Germany) at an accelerating voltage of 3 kV. Formic acid was used to dissolve the matrix resin PA66 selectively from the blends. TLCP particles were separated by centrifugation of the solution and decanting of the supernatant liquid. This procedure was repeated more than five times. The clean TLCP residue was dried for scanning electron microscopy (SEM) observation. The diameters of the TLCP particles were measured from the SEM micrographs artificially, and the average diameter and distribution for one sample were obtained from at least 200 particles.

For polarized optical microscopy observation, thin sections 5 μm in thickness cut at room temperature with a Leica FC7-UC7 microtome were used. Polarized optical microscopy was performed on a Leica DM2500P polarizing microscope in a reflected-light mode.

Mechanical Tests

The TLCP/PA66 containing extrudates were re-extruded with the Haake Polylab single-screw extruder at 305 °C. The screw speed was fixed at 60 rpm. Then, the extrudates were injection-molded at 270 °C with a pony plunger preplasticizing injection-molding machine (Ruiming Co., Ltd., China). The mold was dumbbell-like and the size of the narrow cross section was 5×2 mm^2. The tensile strength and Young's modulus of the injection-molded samples were measured with a universal tensile tester (CMT4104, Shenzhen Sans Testing Machine Co., Ltd., China). The tests were carried out at a crosshead speed of 2 mm/min. The relative humidity and temperature in the test environment were 50 ± 10% and 25 ± 2 °C, respectively. The average value of at least five tests was reported.

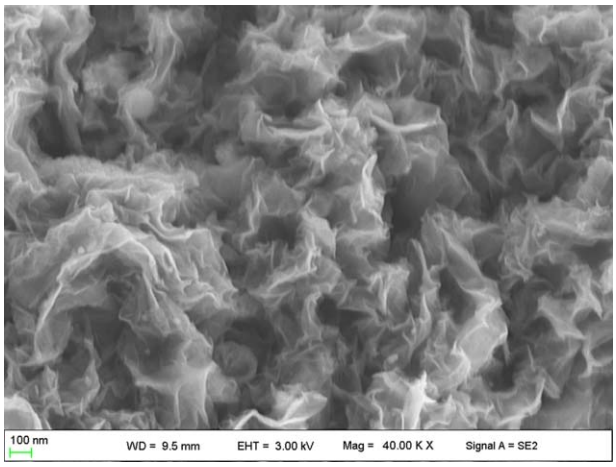

Figure 1. SEM micrograph of the RGO powder. [Color figure can be viewed in the online issue, which is available at wileyonlinelibrary.com.]

RESULTS AND DISCUSSION

Characterization of RGO

RGO was synthesized from the reduction of GO with hydrazine hydrate. Freeze-dried RGO powder was used for further tests and melt blending. Figure 1 is the SEM micrograph of the RGO powder. It was clear that the incompact RGO nanosheets were wholly exfoliated and stacked chaotically. The average size of the planar RGO nanosheets was at most 400 nm, and the space between two single nanosheets was around the tens of nanometers. As shown in Figure 2, the X-ray diffraction patterns illustrated that the RGO powder was amorphous because of its flat diffraction curve compared with the sharp diffraction peak (002) of graphite located at 26.5°. The results of X-ray diffraction corresponded with the aggregation state of the RGO nanosheets (Figure 1). Figure 3 shows the Fourier transform infrared spectra of the precursor GO and RGO. The absorption bands of both RGO and GO around 3422, 1562, and 1101 cm^{-1} were ascribed to the characteristic signals of hydroxyl O—H, ether

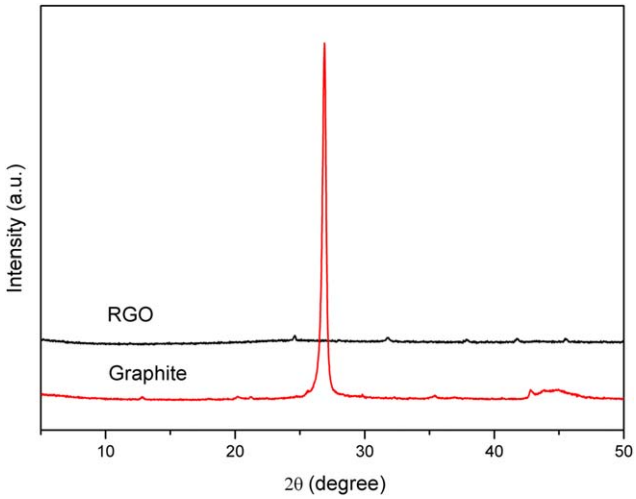

Figure 2. X-ray diffraction patterns of the RGO and graphite. [Color figure can be viewed in the online issue, which is available at wileyonlinelibrary.com.]

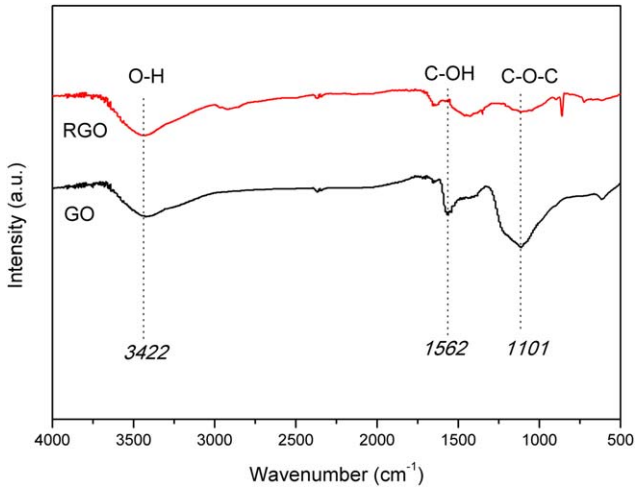

Figure 3. Fourier transform infrared spectra of RGO and GO. [Color figure can be viewed in the online issue, which is available at wileyonlinelibrary.com.]

bond C—OH, and epoxy group C—O—C, respectively. In contrast with GO, the absorption peaks of the ether bond and epoxy group of RGO weakened markedly; this indicated RGO was composed of fewer epoxy groups and alcoholic hydroxyls, whereas the absorption peaks of hydroxyls and carbonyls (roughly 1648 cm^{-1}) showed no decisive changes. This demonstrated that RGO still had some oxygen-containing groups. This was consistent with relative reports[32] that hydrazine hydrate cannot reduce the carboxyls of GO effectively. TGA curves (Figure 4) were used to quantify the reduction degree of RGO. An incipient mass loss near 300 °C was observed for RGO because of the decomposition of the residual oxygen-containing groups after chemical reduction. The temperature at the maximum decomposition rate was roughly 418 °C; this was largely beyond the processing temperature of the blends. According to that, the weight and structure of RGO showed no essential changes during melt blending.

Rheological Behaviors of the Neat Polymers and Their Blends

The rheological tests were performed on a torque rheometer equipped with a capillary extruder (hereafter, referred to as the capillary torque rheometer). In contrast with other kinds of rheometers, the actual rheological behaviors in industrial processes were simulated by the capillary torque rheometer to the largest extent, such as extrusion molding and injection molding. The disadvantage is, of course, that the shear rate (γ) cannot be set at any value required in an experiment because there is no constant quantitative relationship between γ and the screw speed.

Logarithmic plots for the viscosity of the neat polymers and polymer blends with or without RGO are illustrated as a function of γ (Figure 5). Polyamides are typically low-viscous TP matrixes; this causes trouble for the fibrillation of the TLCP phase within them. However, the viscosity of polyamides is insensitive to temperature. Figure 5(a) shows that the viscosity of PA66 was slightly higher than that of TLCP at 285 °C. However, the difference in the viscosities between two polymers increased markedly, especially at high γs, when the temperature increased to 305 °C. Therefore, to obtain a suitable λ, 305 °C was selected for the following rheological measurements. The pseudoplasticity was demonstrated for both PA66 and TLCP in the measured range of γ, that is, from the order of magnitude of 10^2 to 10^3 s^{-1}. More remarkable shear-thinning behavior was noticed for TLCP compared with PA66. The rheological properties of PA66 in this study were consistent with reports elsewhere.[33] PA66 exhibited a noticeable non-Newtonian behavior when γ exceeded 10^3 s^{-1}.

Figure 5(b) illustrates the viscosity of the TLCP/PA66 containing blends with different RGO contents at 305 °C. With the addition of 10 wt % TLCP, the viscosity of blends decreased obviously; this indicated that TLCP acted as a processing agent. However, the viscosity of the binary blends was greater than that of neat TLCP. When RGO was added to the blends, the viscosities decreased further. For the TLCP/RGO(1)/PA66 blend (the figure in the bracket is the weight percentage of RGO to TLCP instead of all of the components; the same applies to future notations), the viscosity was lower than that of the neat TLCP within the full range of γ. The viscosity for the TLCP/RGO(2)/PA66 blend was even as low as 16.7 Pa s; this corresponded to a γ of 1914 s^{-1} at 60 rpm. When RGO rose to 0.3 wt %, there existed a distinct melt fracture at high γs. The surfaces of the extrudates were rugged and even broken. Thus, the rheological data for the TLCP/RGO(3)/PA66 blend were abnegated.

Morphology Evolution of the Dispersed TLCP Phase in the Polymer Blends

The samples were the extrudates of binary TLCP/PA66 blends and ternary TLCP/RGO/PA66 blends performed on the capillary torque rheometer. The final morphology of the TLCP blends depended on several factors, including the processing parameters, properties of component polymers, and compositions of the blends. In this study, we were most concerned with the γ and filler content, and the other factors were kept constant.

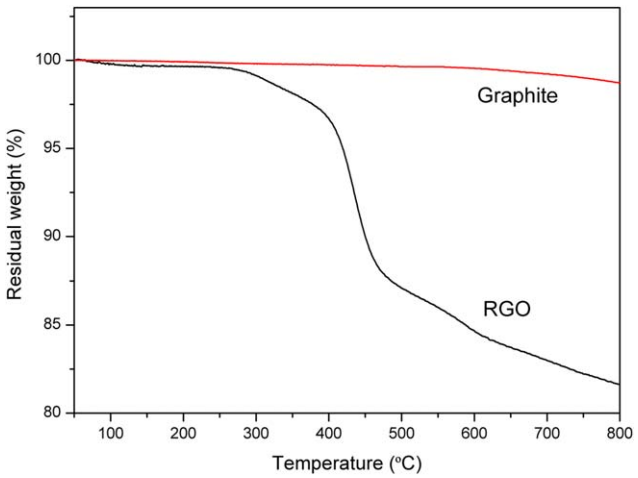

Figure 4. TGA plots of the RGO powder and graphite. [Color figure can be viewed in the online issue, which is available at wileyonlinelibrary.com.]

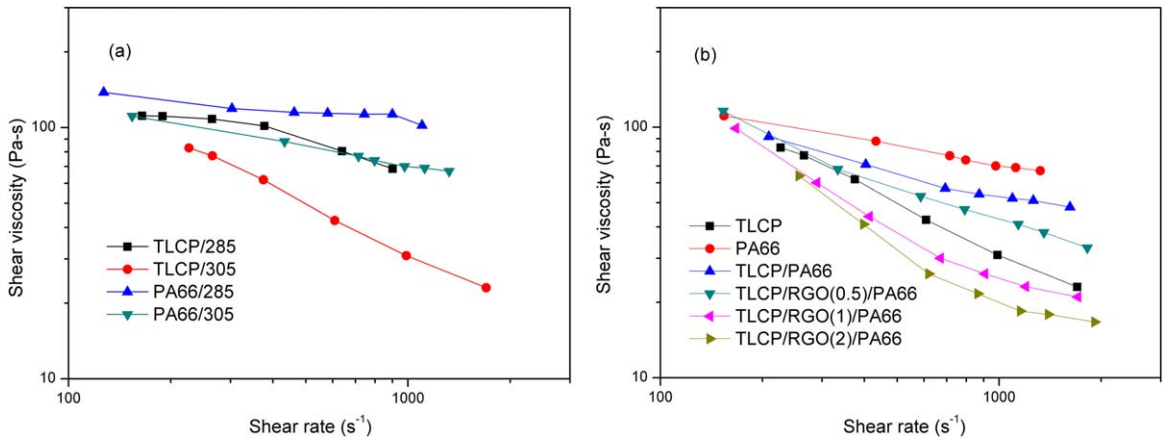

Figure 5. γ dependence of the viscosity for the neat polymers and their blends: (a) neat polymers at 285 and 305 °C and (b) TLCP/PA66-containing blends with various RGO contents at 305 °C. [Color figure can be viewed in the online issue, which is available at wileyonlinelibrary.com.]

Figure 6 shows SEM micrographs of fracture surfaces for the binary TLCP/PA66 blends extruded at different γs. It was clear that the TLCP domains were all spherical at 209 s^{-1}. When γ rose to 693 s^{-1}, a few TLCP domains deformed into fibrils. With increasing γ, more fibrils developed, and the spherical particles gradually disappeared. Apparently, high γs enhanced the fibrillation of the TLCP phase. However, a portion of spherical particles still remained [Figure 6(d)], even though γ reached 1618 s^{-1}.

The locally magnified morphology of a fibril in Figure 6(d) is presented (Figure 7). To our surprise, there existed a hierarchical structure in the TLCP fibril. It was clear that the root segment of the fibril consisted of tens of microfibrils. The diameters of the fibrils and microfibrils were on the order of magnitude of 10^2 and 10^1 nm, respectively. Such a hierarchical structure was found in the spun, extruded, and molded samples of the neat TLCP resin according to earlier reports.[34,35] The

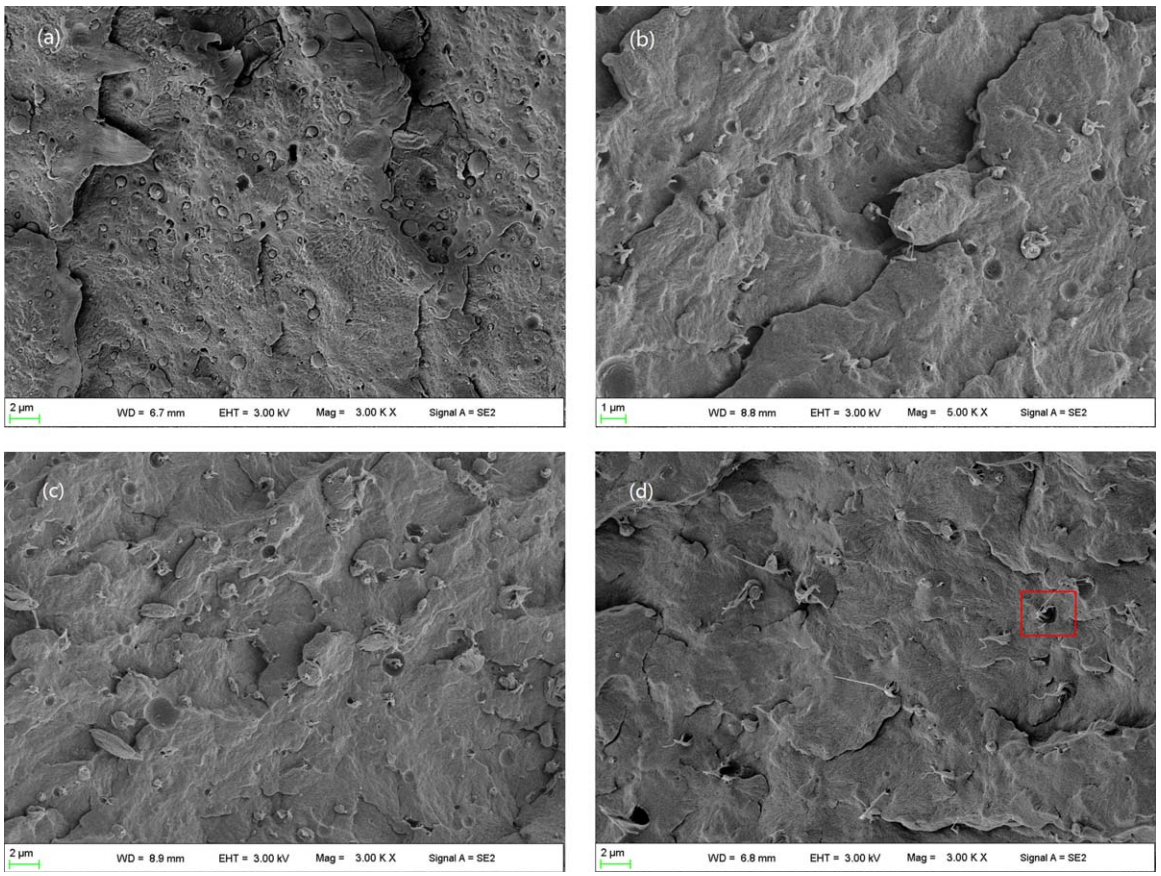

Figure 6. SEM micrographs of the fracture surfaces of the binary TLCP/PA66 blends extruded at (a) 209, (b) 693, (c) 1094, and (d) 1618 s^{-1}. [Color figure can be viewed in the online issue, which is available at wileyonlinelibrary.com.]

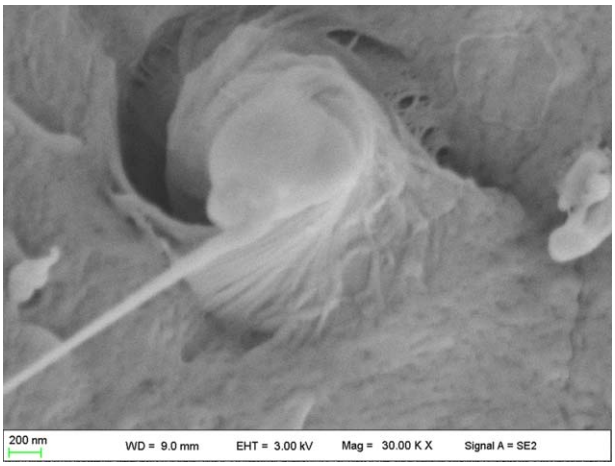

Figure 7. Locally magnified morphology (rotated 180° for a better view) of a fibril labeled in Figure 6(d). [Color figure can be viewed in the online issue, which is available at wileyonlinelibrary.com.]

difference is, unlike the closely aligned microfibrils in neat TLCP, that the microfibrils here were pulled out from the TLCP melt and twisted into fibrils by some strong torsional stress. Ding *et al.*[13] found a similar phenomenon in a ternary TLCP/glass bead/PA6 blend. They suggested that the strong extensional flow field formed by the microrollers of glass beads exerted strong extensional action on TLCP coils; this resulted in the formation of TLCP microfibrils, which were usually generated in the neat TLCP melt only. Extensional flow was supposed to be a more effective method for promoting the fibrillation of TLCP droplets in contrast with shear flow. Obviously, the previous explanation did not apply in this study.

Still, it must be noted that it was the capillary torque rheometer instead of the capillary rheometer that was used in this study. The former was screw-driven, and the latter was plunger-driven. Figure 8 shows their schematics. The plunger of the capillary rheometer could provide a uniform and rectilinear driving force to squeeze the melt into the capillary so that stable laminar flow formed. The driving force in the capillary torque rheometer derived from screw rotation was complicated. The deflective force imposed on the melt could produce an unstable flow. When the unstable flow was too severe to die away before entering the capillary [Figure 8(a)], it could be enhanced and then converted into transition flow or turbulence because of the abrupt rise in the flow velocity in the capillary. Given the fewer chain entanglements internally (i.e., the low melt strength), TLCP droplets were impressionable to external disturbance. Summarizing the previous analysis and the morphology of the TLCP fibrils (Figures 6 and 7), we believe that it was the extensional and torsional action of the unstable flow in the capillary that resulted in the hierarchical structure of TLCP in the binary TLCP/PA66 blends.

Figure 9 shows the SEM micrographs of the fracture surfaces for the ternary TLCP/RGO/PA66 blends with various RGO contents extruded at 60 rpm. Their $\dot{\gamma}$s ranged between 1600 and 2000 s^{-1}. In contrast with those shown in Figure 6(d), the fibrils were more uniform and possessed a larger aspect ratio with increasing RGO content. With the incorporation of 0.05 wt % RGO, there were still a few spherical particles [Figure 9(a)]. Once RGO exceeded 0.1 wt %, almost all of the TLCP particles deformed into fibrils [Figure 9(b–d)]. Undoubtedly, RGO enhanced the fibrillation of the TLCP phase.

Figure 10 shows locally magnified micrographs of the fracture surfaces for the TLCP/RGO/PA66 blends with various RGO contents extruded at two different screw speeds. The RGO contents were 0.05, 0.1, and 0.3 wt %, and the screw speeds were 5 and 60 rpm, respectively. It was noteworthy that the hierarchical structure of the TLCP fibrils could only be observed at high $\dot{\gamma}$s. At 5 rpm, corresponding to $\dot{\gamma}$s ranging between 150 and 250 s^{-1}, no fibrils developed until RGO exceeded 0.1 wt %. The straight and unitary fibrils [Figure 10(c,e)] demonstrated that there existed stable shear flow at low $\dot{\gamma}$s. However, unstable flow and even turbulence gradually emerged with mounting $\dot{\gamma}$s. According to the morphological evolution of the fibrils (Figure 9) and microfibrils [Figure 10(b,d,f)], there were signs that the addition of RGO aggravated the unstable flow (i.e., the extensional and torsional action). Such supposition echoed the rheological tests (Figure 5). When RGO rose up to 0.3 wt %, the extrudates became rough and accidented at high $\dot{\gamma}$s. However, there was no distinct melt fracture in the binary TLCP/PA66 blends. The melt fracture in this study was mainly attributed to the unstable flow in the capillary and the melt viscoelasticity of the polymer components. Because of the structural differences (Figure 8), we supposed that the critical $\dot{\gamma}$ in the capillary rheometer was greater than that in the capillary torque rheometer for the same sample under the same conditions.

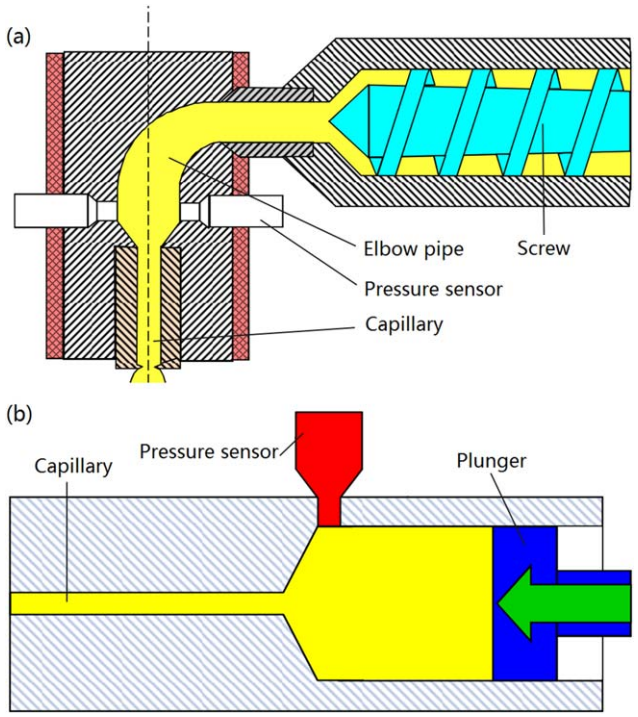

Figure 8. Schematics of the (a) capillary torque rheometer and (b) capillary rheometer. [Color figure can be viewed in the online issue, which is available at wileyonlinelibrary.com.]

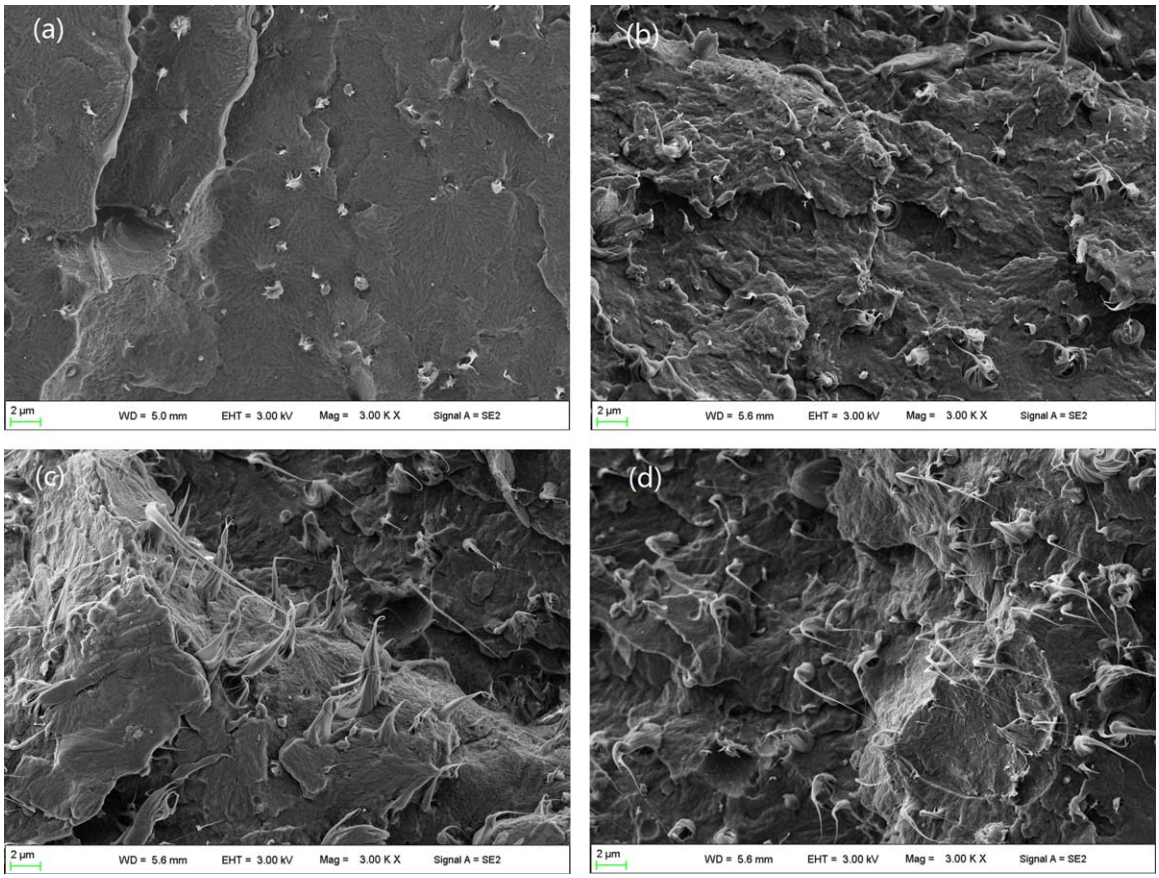

Figure 9. SEM micrographs of the fracture surfaces of the ternary TLCP/RGO/PA66 blends extruded at 60 rpm with increasing RGO contents of (a) 0.05, (b) 0.1, (c) 0.2, and (d) 0.3 wt %. γs for the four blends ranged roughly from 1600 to 2000 s^{-1}. [Color figure can be viewed in the online issue, which is available at wileyonlinelibrary.com.]

Effect of RGO on the Mechanical Properties of the TLCP/RGO/PA66 Composites

As promising structural materials, good mechanical performances are required for TLCP blends, although the strength of most TLCP/TP composites does not act up to the rule of mixture,[14] especially at a low TLCP contents; this is attributed to the bad compatibility between the matrixes and TLCPs, the inhomogeneity of the disperse phase, defective fibrillation, and so on.

Microfibrils are the finest fibrillar species in TLCP blends.[13,34] To examine the enhancing effect, injection-molded samples were tested. Figure 11 shows the tensile strength and tensile modulus for the binary PA66/RGO blends and ternary TLCP/RGO/PA66 blends. When RGO exceeded 0.05 wt %, a significant improvement in both the tensile strength and modulus was obtained for ternary blends. However, the mechanical performances for the unfilled TLCP/PA66 blends degraded compared to that of neat PA66. Through the dissolution of samples with formic acid and observation of the morphology of the residuals (the figure is not given here), we found that the percentage of fibrillation for unfilled blends was rather low; this caused a separate and impaired matrix and, thus, led to a decrease in the tensile strength. TLCPs and TPs were thermodynamically incompatible with weak interfacial interactions. Consequently, the addition of TLCP to TP matrixes usually results in a significant increase in the modulus but only a slight increase in the strength.[13,36]

Compatibilization Effect of RGO on the Immiscible Polymer Blends

The previous results indicate that RGO indeed enhanced the fibrillation of the TLCP phase in the PA66 matrix. Two approaches were supposed in the implementation process. One was the extensional and torsional action of the unstable flow aggravated by RGO; this was confirmed by the rheological tests (Figure 5). The other was the enhanced interfacial interactions between the TLCP droplets and PA66 matrix by RGO.

Polymer blending is a process that makes the minor phase dispersed uniformly into the matrix in the desired domain shape and size. The morphological evolution is dynamic, including the deformation, breakup, collision (thereby coalescence), and relaxation. For the binary TLCP/TP blends, two basic rheological parameters were crucial to the deformation and fibrillation of the dispersed TLCP phase. They are λ of the dispersed phase to the matrix, η_d/η_m, η_d denotes the viscosity of the dispersive phase, η_m denotes the viscosity of matrix and the capillary number (Ca).[21] An essential condition for fibrillation is that λ be less than unity at a low TLCP content.[37] Ca is defined as the ratio of the shear stress acting on the TLCP droplet by an

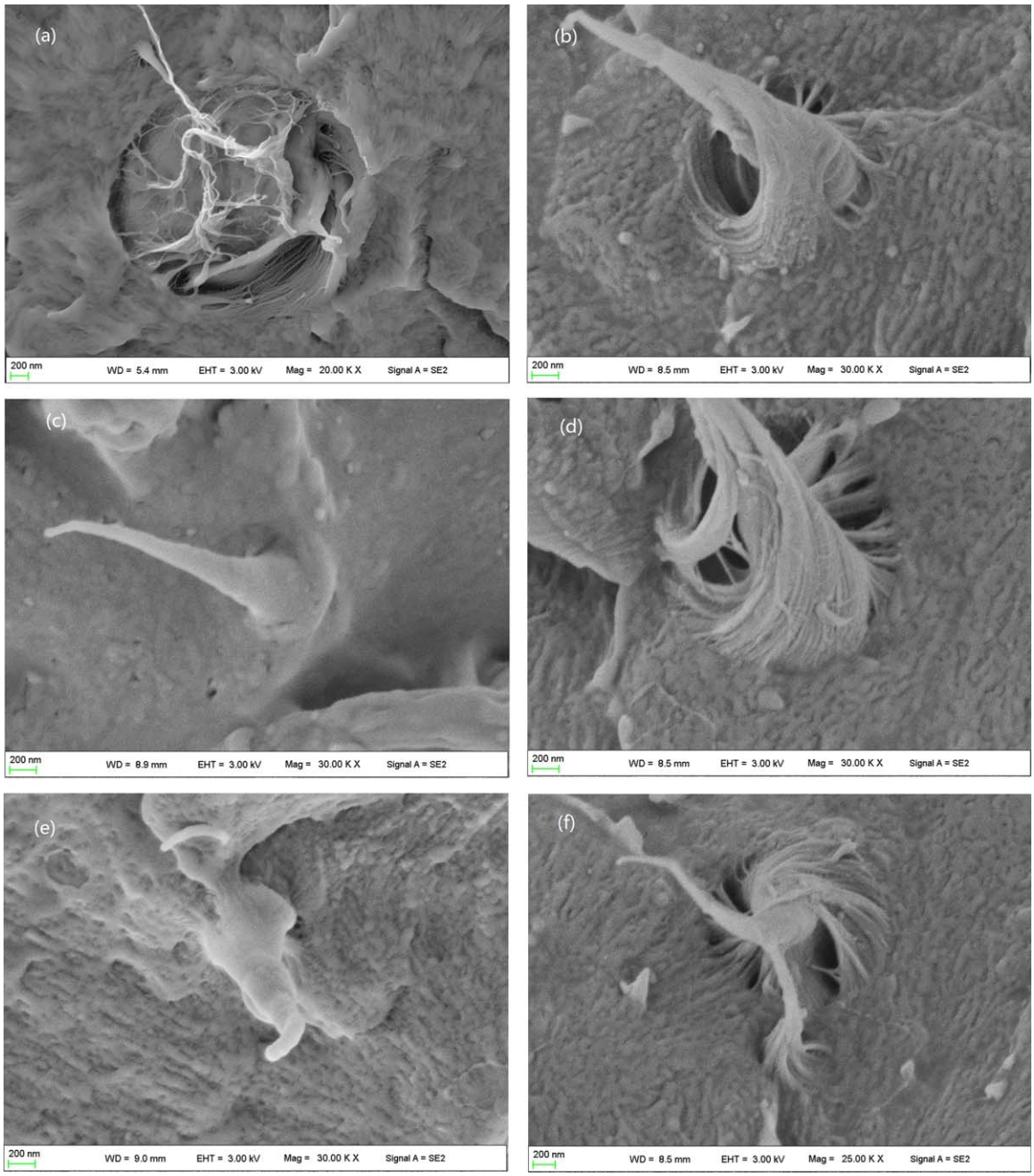

Figure 10. Locally magnified micrographs of the fracture surfaces of the TLCP/RGO/PA66 blends extruded at two different screw speeds [(left) 5 rpm ($\gamma = 150$–$250\ s^{-1}$) and (right) 60 rpm ($\gamma = 1600$–$2000\ s^{-1}$)]: (top) 0.05 wt % RGO, (center) 0.1 wt % RGO, and (bottom) 0.3 wt % RGO. [Color figure can be viewed in the online issue, which is available at wileyonlinelibrary.com.]

external flow field to the interfacial tension which resists the deformation of the spherical droplet. In the simple shear flow, it is formulated as

$$Ca = \frac{\text{Hydrodynamic stress}}{\text{Interfacial stress}} = \frac{\eta_m \gamma}{\frac{\sigma}{R}} \quad (1)$$

where R is the droplet radius and σ is the interfacial tension of polymer pairs. There is a critical capillary number (Ca_{crit}), beyond which the droplet cannot sustain continuous deformation and will eventually break up. λ dependence of Ca_{crit} for the simple shear flow can be calculated from an empirical equation:[38]

$$\log(Ca_{crit}) = -0.5060 - 0.0994 \log\lambda + 0.1240(\log\lambda)^2 - \frac{0.1150}{\log\lambda - 0.6110} \quad (2)$$

On the basis of mathematical calculation, Ca_{crit} was nearly constant (roughly 0.46) when the λs ranged from 0.1 to 1. In theory, TLCP droplets will deform into long stable filaments in the matrix when Ca/Ca_{crit} exceeded 4.[38] Zhang *et al.*[21] found that all TLCP droplets should deform into fibrils in shear flow, provided γ exceeds 120 s^{-1} in binary Vectra A950 (TLCP)/PA6 systems. However, no fibrils were generated during melt

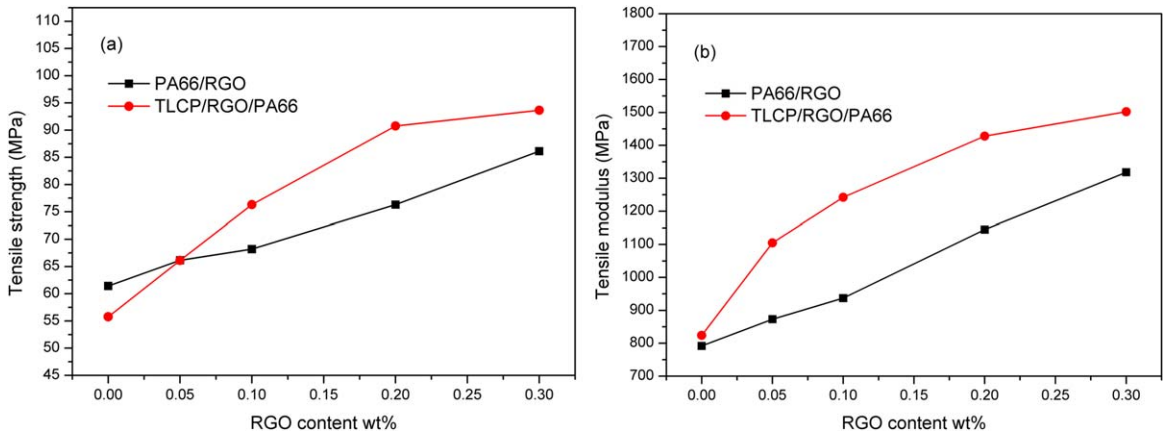

Figure 11. (a) Tensile strength and (b) tensile modulus as a function of the RGO content for the PA66/RGO blends and TLCP/RGO/PA66 blends. [Color figure can be viewed in the online issue, which is available at wileyonlinelibrary.com.]

extrusion, where γ even reached 1000 s^{-1} in the die. They stated that there existed serious interfacial slip between the TLCP droplets and PA6 matrix resulted from the low chain entanglements at the interface of two immiscible polymers.

In our study, fibrils and macrofibrils were found at high γs in the binary TLCP/PA66 blends (Figure 6), and it was attributed to the extensional and torsional action of unstable flow. The simple shear flow was formed only at low γs for the capillary torque rheometer. Because of the interfacial slip between two polymer components, the shear stress transferred to the TLCP droplets was insufficient to overcome the interfacial tension so that no fibrils developed in the simple shear flow. However, the straight and unitary fibrils [Figure 10(c,e)] generated by the simple shear flow in the ternary TLCP/RGO/PA66 blends demonstrated that the interfacial interactions between TLCP and PA66 phase were enhanced by RGO.

The enhanced interfacial interactions could be further proved by the dimensional changes of the dispersive TLCP droplets during melt processing. When the interfacial adhesion between the TLCP and matrix was improved, the tumble and slippage of the TLCP droplets were suppressed so that more energy could be used for the breakup and deformation, and this led to a significant decrease in the size. The blends taken from the barrel of the capillary torque rheometer were corroded with formic acid to remove the soluble PA66 matrix. The morphology of the TLCP particles is illustrated in Figure 12. Most particles were spherical or ellipsoidal; this showed that the shear stress of the screw in the barrel could hardly fibrillate the TLCP droplets. Table I summarizes the statistics on the number-average diameters of the spheres. The spheres in the binary TLCP/PA66 blends were the largest, with an average diameter of 6.9 μm. With the incorporation of RGO, the average diameter of the TLCP spheres began to decrease remarkably. In the TLCP/RGO(3)/PA66 blend, the average diameter was as low as 2.7 μm. Similar findings that nanofillers decreased the size of the TLCP droplets in the TLCP/TP blends were also reported in the TLCP (Vectra A950)/nanoclay/PA6 blends.[21]

Analysis of the Compatibilization Mechanism

To figure out the mechanism of the compatibilization of RGO, one must determine in which phase RGO is located during melt blending. It has been reported that the selective distribution of nanofillers exerted a great influence on the morphology of thermodynamically immiscible polymer blends.[37,39,40] The filler distribution was determined by thermodynamic parameters (e.g., the interfacial tension between polymers or between the polymer and filler) and dynamic parameters (e.g., the viscosity of the component polymers).[13,15,39] In filled blends composed of a pair of immiscible polymers, the filler was selectively located in the position where it possessed the lowest interfacial tension.[41] Sumita *et al.*[42] introduced a wetting coefficient (*Wa*) derived from Young's equation to quantifiably predict the selectivity of the filler:

$$Wa = \frac{\gamma_{\text{filler-polymer1}} - \gamma_{\text{filler-polymer2}}}{\gamma_{\text{polymer 1,2}}} \quad (3)$$

where the γ subscripts denote the interfacial tensions between the filler and polymers 1 and 2 and the interfacial tensions between the two polymers. Actually, theoretical predictions are confronted with the difficulty of accurately measuring γ between the nanoparticles and polymer melt because of the indefinite aggregation state of the nanoscaled surfaces of the filler. So is the determination of the accurate surface energy values for RGO. In addition, the surface energy for RGO can change in a large range because of the uncertain reduction degree and the structural defect of RGO. Thus, there were no existing surface energy data to use in this investigation. Apart from the thermodynamic factor discussed previously, the dynamic factor should be taken into consideration as well. In particular, under the circumstance that the affinity of the fillers to both component polymers is similar, the dynamic parameter would be the predominant factor for determining the location of the fillers.

On account of the complexity of the selective distribution of nanofillers, it is not reliable to theoretically predict the localization behavior of nanofillers in a melt-mixed multiphase polymer blend. Experiments and microscopic observation were indispensable. We prepared a ternary TLCP(54)/RGO(1)/PA66(45) blend, where RGO was 1 wt %, and the volume ratio of TLCP to PA66 1 by a two-step mixing process, as discussed previously. The specimen was taken from the barrel of the capillary torque rheometer. Figure 13 shows the polarized optical micrograph of the microsection. It is noteworthy that TLCP and PA66 did not

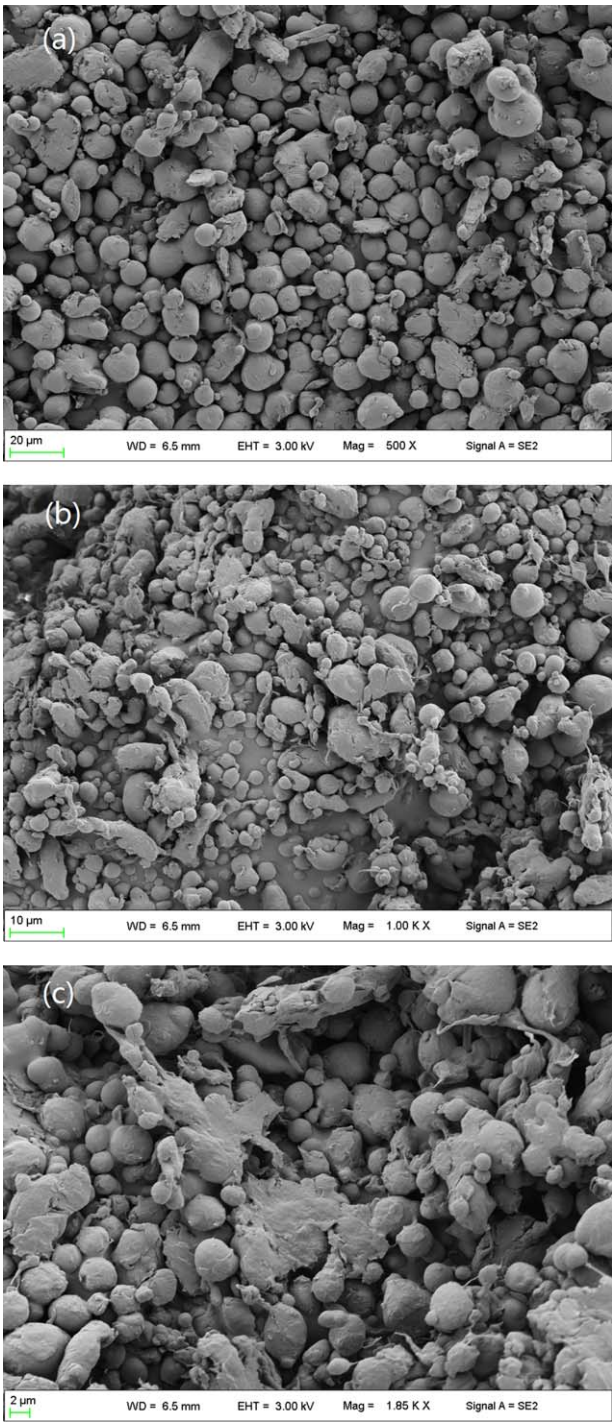

Figure 12. Morphology of the TLCP particles in the (a) binary blends and (b,c) ternary blends with RGO contents of 0.1 and 0.3 wt %, respectively. [Color figure can be viewed in the online issue, which is available at wileyonlinelibrary.com.]

form a cocontinuous structure, even though their volume ratio was 1. PA66 as the continuous phase had a negative curvature, and TLCP as the dispersive phase had a positive curvature. That is, the TLCP melt could not spread on the surface of the PA66 melt, and this possibly indicated a higher surface energy for the TLCP melt. RGO was well dispersed in the blends for only a few agglomerates, as shown in Figure 13. It was clear that some RGO agglomerates were still located in the vicinity of the TLCP phase. Some agglomerates have migrated to the interface between the TLCP and PA66 phase (e.g., red rectangles in Figure 13).

Melt processing is a short-time process, lasting for only several minutes. Fillers might not have enough time to migrate to the expected location in thermodynamic equilibrium, despite the thermodynamic force toward better wetting. Göldel *et al.*[39] introduced the slim fast mechanism to elucidate the transfer mechanism for variform carbon fillers and proposed that the velocity of the filler transfer and the final filler localization were a function of the aspect ratio and the dimension of the filler. According to that, fillers with a high aspect ratio, such as carbon nanotubes, have a higher driving force toward better wetting, whereas fillers with a lower aspect ratio, such as carbon black and possibly graphene, have a higher probability for interfacial localization.

In this study, π–π stacking interactions of TLCP molecules on the graphene plane could form as a result of the high-density benzene rings and naphthalene rings in the molecular structure of Vectra A950.[26,43,44] Meanwhile, according to the results of IR analysis and thermogravimetric analysis (Figures 3 and 4), RGO still comprised considerable oxygen-containing groups, upon which strong hydrogen bonds could form between the RGO nanosheets and PA66 molecules.[32,43] In this case, the RGO nanosheets were amphipathic with a similar affinity to both component polymers. Perhaps the interfacial distribution for RGO possessed the lowest interfacial tension. Therefore, the interfacial interactions of the component polymers were enhanced. The RGO powder was proven incompact and amorphous (Figures 1 and 2), so a good dispersion and even the monolayer dispersion of RGO in blends by melt processing were easily obtained (Figure 13). Although the addition of RGO was rather low, the whole surface coverage of the TLCP droplets was accessible because of the large surface area brought about by the planar structure of the nanoscaled RGO. The RGO nanosheets located in the interface between the TLCP droplets and the PA66 matrix also impeded the coalescence of TLCP droplets caused by collision. This was another reason for the size reduction of the TLCP droplets. Similarly, Yang *et al.*[45] found that GO nanosheets could compatibilize the PA6/PVDF blends by

Table I. Comparison of the Number-Average Diameters and Diameter Distributions of the TLCP Spheres in the Binary and Ternary Blends

RGO content (wt %)	Number-average diameter distribution (%)			Average diameter (μm)
	<2 μm	2–5 μm	>5 μm	
0	7	47	46	6.9
0.05	6	69	25	4.4
0.1	13	71	16	3.2
0.2	13	76	11	3.0
0.3	18	74	8	2.7

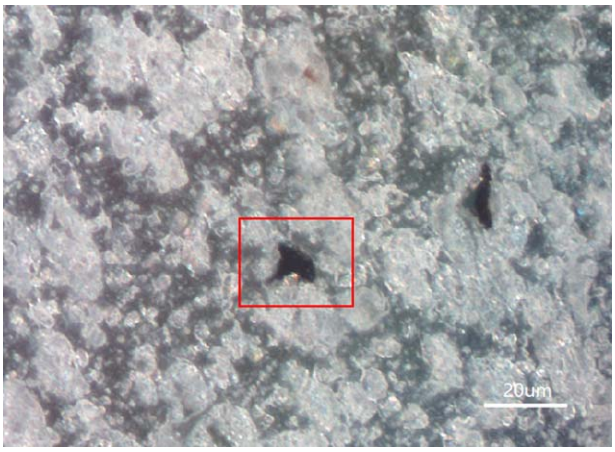

Figure 13. Polarized optical micrograph of a microsection of a ternary TLCP(54)/RGO(1)/PA66(45) blend. The white and translucent sections are the TLCP and PA66 phase, respectively. The atrament labeled in the red rectangle is the RGO agglomerate located in the interface between the two polymers. [Color figure can be viewed in the online issue, which is available at wileyonlinelibrary.com.]

taking advantage of their unique amphipathic structure. They suggested the edge polar groups of GO-formed hydrogen bonds with PA6, whereas the basal planar of GO interacted with electron-withdrawing fluorine on PVDF chains. This led to so-called charge-transfer C—F bonding. Thus, GO exhibited favorable interactions with both PA6 and the PVDF phase; this minimized the interfacial tension.

The rheological properties of the blends were correlated with the morphology of TLCP.[25] With the addition of stiff TLCP, the PA66 matrix was lubricated because of the fewer chain entanglements between two polymers. The viscosity of the blends could be further reduced only when the TLCP-formed fibrils.[12] In the binary TLCP/PA66 blends, the fibrils began to develop only at high γs, and the viscosity slightly decreased. With the incorporation of RGO, more TLCP droplets fibrillated because of the enhanced interfacial interactions, and then, the viscosity decreased dramatically. On the basis of the theory of fluid mechanics,[46] for low viscous liquids, this was more likely to induce an unstable flow; this, in turn, generated more fibrils by extensional and torsional action. Finally, the reciprocal causation between fibrillation and viscosity reduction brought about melt fracture.

CONCLUSIONS

With a capillary torque rheometer, binary TLCP/PA66 blends and ternary TLCP/RGO/PA66 blends were prepared. As a pair of immiscible polymers, there existed interfacial slip between TLCP (Vectra A950) and PA66 so that no fibrils developed in the simple shear flow. The addition of RGO nanosheets enhanced the interfacial interactions because of their amphipathic structure. The size of TLCP droplets decreased markedly with increasing RGO content. TLCP droplets began to fibrillate at low γs when RGO exceeded 0.1 wt %. The fibrillation further brought about a sharp decrease in the viscosity of the blends, whereas the melt fracture occurred in the low-viscous blends when γ rose to the order of magnitude of 10^3 s^{-1}.

The hierarchical structures of the TLCP fibrils were both found in binary and ternary blends. Microfibrils were pulled out from the periphery of the TLCP droplets and twisted into fibrils by extensional and torsional action of unstable flow in capillary. The unstable flow was possibly derived from the unique structure of the capillary torque rheometer and low intermolecular viscous force of TLCP. The mechanical performances of the ternary blends were enhanced because of the improved fibrillation of TLCP by RGO nanosheets.

REFERENCES

1. Kiss, G *Polym. Eng. Sci.* **1987**, *27*, 410.
2. Lee, M. W.; Hu, X.; Yue, C. Y.; Li, L.; Tam, K. C.; Nakayama, K. *J. Appl. Polym. Sci.* **2002**, *86*, 2070.
3. Kim, S. Y.; Kim, S. H.; Lee, S. H.; Youn, J. R. *Compos. A* **2009**, *40*, 607.
4. McLeod, M. A.; Baird, D. G. *Polymer* **1999**, *40*, 3743.
5. Hsieha, T.; Tiua, C.; Simonb, G.; Wu, R. Y. *J. Non-Newtonian Fluid Mech.* **1999**, *86*, 15.
6. Saengsuwan, S.; Mitchell, G. R.; Bualek-Limcharoen, S. *Polymer* **2003**, *44*, 5951.
7. Tang, Y. H.; Gao, P.; Ye, L.; Zhao, C. *Polymer* **2010**, *51*, 514.
8. Hatui, G.; Malas, A.; Bhattacharya, P.; Dhibar, S.; Kundu, M. K.; Kumar Das, C. *J. Alloys Compd.* **2015**, *619*, 709.
9. Zhang, J.; He, J. *Polymer* **2002**, *43*, 1437.
10. Tang, Y.; Zuo, M.; Gao, P. *Korea-Aust. Rheol. J.* **2014**, *26*, 303.
11. Gopakumar, T. G.; Ponrathnama, S.; Lele, A.; Rajan, C. R.; Fradetb, A.; Gopakumar, T. G. *Polymer* **1999**, *40*, 357.
12. Zheng, X.; Zhang, J.; He, J. *J. Polym. Sci. Part B: Polym. Phys.* **2004**, *42*, 1619.
13. Ding, Y.; Zhang, J.; Chen, P.; Zhang, B.; Yi, Z.; He, J. *Polymer* **2004**, *45*, 8051.
14. Wang, H.; Lee, K.; Chung, T.; Jaffe, M. *Polym. Compos.* **2000**, *21*, 114.
15. Wu, L.; Chen, P.; Zhang, J.; He, J. *Polymer* **2006**, *47*, 448.
16. Costa, G.; Meli, D.; Song, Y.; Turturro, A.; Valenti, B.; Castellano, M.; Falqui, A. *Polymer* **2001**, *42*, 8035.
17. Tjong, S. C.; Meng, Y. *J. Appl. Polym. Sci.* **1998**, *70*, 1611.
18. Tjong, S. C.; Li, R.; Xie, X. *J. Appl. Polym. Sci.* **2000**, *77*, 1964.
19. Choi, J.; Lee, B.; Choi, Y.; Jo, B.; Choi, S. *J. Appl. Polym. Sci.* **2015**, *132*, 41408.
20. Caligiuri, L.; Stagnaro, P.; Valenti, B.; Canalini, G. *Eur. Polym. J.* **2009**, *45*, 217.
21. Zhang, B.; Ding, Y.; Chen, P.; Liu, C.; Zhang, J.; He, J.; Hu, G. *Polymer* **2005**, *46*, 5385.
22. Kumar, S.; Rath, T.; Mahaling, R. N.; Das, C. K. *Compos. A* **2007**, *38*, 1304.
23. Hong, J. S.; Kim, Y. K.; Ahn, K. H.; Lee, S. J.; Kim, C. *Rheol. Acta* **2006**, *46*, 469.

24. He, J.; Zhang, H.; Wang, Y. *Polymer* **1997**, *38*, 4279.
25. Gao, P.; Mackley, M. R.; Zhao, D. *J. Non-Newtonian Fluid Mech.* **1999**, *80*, 199.
26. Sun, X.; Sun, H.; Li, H.; Peng, H. *Adv. Mater.* **2013**, *37*, 5153.
27. Lee, C.; Wei, X.; Kysar, J. W.; Hone, J. *Science* **2008**, *321*, 385.
28. Kalaitzidou, K.; Fukushima, H.; Drzal, L. T. *Carbon* **2007**, *45*, 1446.
29. Lee, S.; Kim, M. S.; Naskar, A. K.; Ogale, A. A. *Polymer* **2005**, *46*, 2663.
30. Marcano, D. C.; Kosynkin, D. V.; Berlin, J. M.; Sinitskii, A.; Sun, Z.; Slesarev, A. *ACS Nano* **2010**, *4*, 4806.
31. Zhu, Y.; Murali, S.; Cai, W.; Li, X.; Suk, J. W.; Potts, J. R.; Ruoff, R. S. *Adv. Mater.* **2010**, *22*, 3906.
32. Loh, K. P.; Bao, Q.; Ang, P. K.; Yang, J. *J. Mater. Chem.* **2010**, *20*, 2277.
33. Ceccia, S.; Cocquet, C.; Trouillet-Fonti, L.; Long, D. R. *Rheol. Acta* **2014**, *53*, 181.
34. Weng, T.; Hiltener, A.; Baer, E. *J. Mater. Sci.* **1986**, *21*, 744.
35. Sawyer, L. C.; Jaffe, M. *J. Mater. Sci.* **1986**, *21*, 1897.
36. Jang, S. H.; Kim, B. S. *Polym. Eng. Sci.* **1994**, *34*, 847.
37. Elias, L.; Fenouillot, F.; Majeste, J. C.; Cassagnau, P. *Polymer* **2007**, *48*, 6029.
38. Huneault, M. A.; Shi, Z. H.; Utracki, L. A. *Polym. Eng. Sci.* **1995**, *35*, 115.
39. Göldel, A.; Marmur, A.; Kasaliwal, G. R.; Pötschke, P.; Heinrich, G. *Macromolecules* **2011**, *44*, 6094.
40. Nayak, G. C.; Sahoo, S.; Rajasekar, R.; Das, C. K. *Compos. A* **2012**, *43*, 1242.
41. Premphet, K.; Horanont, P. *Polymer* **2000**, *41*, 9283.
42. Sumita, M.; Sakata, K.; Asai, S.; Miyasaka, K.; Nakagawa, H. *Polym. Bull.* **1991**, *25*, 265.
43. Terrones, M.; Martín, O.; González, M.; Pozuelo, J.; Serrano, B.; Cabanelas, J. C.; Baselga, J. *Adv. Mater.* **2011**, *23*, 5302.
44. Shen, B.; Zhai, W.; Tao, M.; Lu, D.; Zheng, W. *Compos. Sci. Technol.* **2013**, *86*, 109.
45. Yang, J.; Feng, C.; Dai, J.; Zhang, N.; Huang, T.; Wang, Y. *Polym. Int.* **2013**, *62*, 1085.
46. Vergnes, B. *Int. Polym. Proc.* **2015**, *30*, 3.

SGML and CITI Use Only
DO NOT PRINT